



Encaging Co nanoparticle in atomic Co—N₄-dispersed graphite nanopocket evokes high oxygen reduction activity for flexible Zn-air battery

Yuandong Yang ^{a,1}, Yi Xiao ^{b,1}, Linjie Zhang ^{b,*}, Hsiao-Tsu Wang ^c, Kuan-Hung Chen ^d, Wei-Xuan Lin ^d, Na Jin ^b, Chen Sun ^b, Yu-Cheng Shao ^e, Jeng-Lung Chen ^e, Jinjie Qian ^{a,*}, Lili Han ^{b,*}

^a College of Life and Environmental Science & College of Chemistry and Materials Engineering, Wenzhou University, Wenzhou 325035, Zhejiang, China

^b State Key Laboratory of Structural Chemistry, Fujian Institute of Research on the Structure of Matter, Chinese Academy of Sciences, Fuzhou 350002, China

^c Bachelors's Program in Advanced Materials Science, Tamkang University, New Taipei City 251301, Taiwan

^d Department of Physics, Tamkang University, New Taipei City 25137, Taiwan

^e National Synchrotron Radiation Research Center, Hsinchu 30076, Taiwan



ARTICLE INFO

Keywords:

Metal-organic framework
Graphite nanopocket
Single-atom catalyst
Oxygen reduction reaction
Synergistic electrocatalysis

ABSTRACT

Rational design of oxygen reduction reaction (ORR) electrocatalysts with indestructible active sites for high-performance Zn-air batteries (ZABs) remains a significant challenge. Herein, we achieve an innovative active site design by encaging Co nanoparticles within the Co—N₄ atomic sites-dispersed graphite nanopocket (Co_{SAs}-NPs/NC), leading to outstanding alkaline ORR activity and stability, and consequently ultra-high power density of 193.8 mW cm⁻² and specific capacity of 819.1 mAh g_{Zn}⁻¹ at 10 mA cm⁻² of a primary ZAB assembled, along with impressive power density of 73.4 mW cm⁻² and charging/discharging stability up to 110 cycles of a flexible solid-state ZAB. Theoretical calculations unveil the enhanced ORR kinetics can be traced to the significantly optimized local electronic structure of Co—N₄ sites with upshifted d-band center and reduced energy barrier of rate-limiting step by the encaged Co nanoparticle. This study showcases a creative conformational design for guiding the construction of valid synergy in hybridized metal/single-atom catalysts.

1. Introduction

In recent years, the rapid advancement of health monitoring systems, sensors, smart display units, and wearable electronic devices has underscored the urgent need for an advanced class of energy conversion devices to provide power to these aforementioned devices [1–3]. There is a strong emphasis on energy storage devices that possess high energy density, excellent conversion efficiency, long-term stability, superior bending resistance and high safety. Flexible Zn-air batteries (ZABs) not only meet these criteria but also offer a promising option for environmentally friendly energy storage due to their simple assembly process, cost-effectiveness and eco-friendly nature [4–6]. However, despite these advantages, the sluggish kinetics of the oxygen reduction reaction (ORR) at the cathode significantly impedes its industrial implementation [7–9]. Platinum (Pt)-based catalysts are widely recognized as highly efficient ORR electrocatalysts due to their exceptional electrocatalytic activity

and selectivity compared to other ORR catalysts [10,11]. Nevertheless, their large-scale application is constrained by their high cost, limited natural availability, poor stability and vulnerability to poisoning. Therefore, the development of highly active yet durable and affordable ORR catalysts with intricately engineered active sites remains a challenging task [12–14].

Currently, transition metal-based M—N—C (M = Fe, Co, Ni, Mn, etc.) type single-atom catalysts (SACs) with hemoglobin-mimicking cores have emerged as promising alternatives to Pt-based catalysts due to their high atom utilization and ORR activity [15–19]. However, the limited loading of single-atom active centers in most SACs results in a limited number of active sites for O-containing intermediates during the ORR process, which restricts the reaction kinetics [20,21]. Moreover, repeated charging and discharging reactions within the electrolyte can cause passivation of the single-atom active centers, thereby compromising the stability of SACs. Therefore, there is a pressing need for novel

* Corresponding authors.

E-mail addresses: zhanglinjie@fjirsm.ac.cn (L. Zhang), jinjieqian@wzu.edu.cn (J. Qian), llhan@fjirsm.ac.cn (L. Han).

¹ These authors contributed equally to this work.

strategies to develop SACs with enhanced intrinsic activity and stability [22–24]. In recent years, carbon-based SACs derived from metal-organic frameworks (MOFs) have shown remarkable advancements in ORR electrocatalysis due to their tunable morphologies, developed pore structures, customizable metal single-atom centers and local coordination configurations [25–27]. Nevertheless, the electrocatalytic performance of these MOF-derived SACs is often compromised by the symbiotic metal nanoparticles (NPs) formed during high-temperature MOF-pyrolysis, which generally exhibit inferior ORR activity and stability due to the leaching in electrocatalysis [28–30]. Recent intensive studies have emphasized on the synergistic ORR electrocatalysis between the SACs and corresponding metal NPs, arguing that the nearby NPs contribute to ameliorated electronic structures of single-atom sites and consequent much improved intrinsic ORR activity, which can overcome the low loading problem of SACs in catalysis [31–33]. However, a commonly overlooked issue when examining these reported catalysts is the inherent weakness and instability of this synergy. As the single-atom (SA) sites are not concentrated around the NPs, a significant portion of the NP surfaces remains spare, leading to an inefficient and underutilized synergy. Moreover, these NPs are typically not confined within the carbon scaffold and directly exposed to the electrolytes, which will cause inevitable metal leaching under the electrocatalytic conditions, rendering a gradually weakened synergy between the SA sites and NPs for ORR. To this end, it is highly desirable to pursue creative structural designs to MOF-derived SACs-NPs coexisting catalysts with substantial as well as strong and sturdy synergistic sites.

In this study, we present the design and synthesis of an intriguing $\text{Co}_{\text{SAs-NPs}}/\text{NC}$ catalyst from a well worked out MOF-based synthetic route, which comprises small Co-NPs enclosed in few-layer graphite nanopockets modified with Co-SAs. This innovative design maximizes utilization of Co-NPs by intimately building Co-SAs-loaded graphite walls around them, resulting in optimized synergy between Co-NPs and Co-SAs. This enhances the intrinsic ORR activity of Co-SA while limiting agglomerative deactivation and retarding the oxidative solvation, diffusion, and Ostwald ripening process of both the Co-NPs and Co-SAs. These two unique conformational relationships efficiently enhance the ORR activity and long-term durability of the $\text{Co}_{\text{SAs-NPs}}/\text{NC}$ catalyst. Electrochemical assays reveal an impressive half-wave potential ($E_{1/2}$) of 0.871 V versus reversible hydrogen electrode (RHE), accompanied by a large diffusion-limited current density of 5.81 mA cm^{-2} and superior stability of 20 h with a current retention rate of 96.5%, surpassing those of commercial 20 wt% Pt/C catalyst. Furthermore, the primary liquid zinc-air battery (ZAB) based on the $\text{Co}_{\text{SAs-NPs}}/\text{NC}$ -based exhibits both high power density (193.8 mW cm^{-2}) and specific capacity ($819.1 \text{ mAh g}_{\text{Zn}}^{-1}$). Notably, the catalyst also demonstrates remarkable rechargeable stability in flexible solid-state ZAB, capable of sustained charging and discharging for 110 cycles with a lifetime approaching nearly 50 h. These exceptional performances endorse the use of $\text{Co}_{\text{SAs-NPs}}/\text{NC}$ as a promising alternative to commercial Pt/C in practical flexible ZAB applications serving as highly efficient energy source for powering wearable electronic devices. Additionally, our theoretical simulations further disclose the pivotal role of the strong and sturdy synergy between Co-NPs and Co-SAs in modulating the electronic structure of Co-SAs active sites, which significantly reduces the energy barrier of the rate-determining step for OH^- desorption.

2. Experimental section

2.1. Synthesis of Co-MOF

30 mg of $\text{C}_4\text{H}_6\text{CoO}_4 \cdot 4\text{H}_2\text{O}$ (0.12 mmol) and 33 mg of H_4dobpd (0.12 mmol) were mixed in 9 mL of DMF: MeOH: H_2O : THF (volume ratio 2:1:2:1) mixture solution. Then the mixture was subjected to ultrasonication until all solids were dissolved. Afterwards, it was transferred into a 15 mL Teflon-lined autoclave and placed in a pre-heated oven at 100 °C for 24 h. After natural cooling, the purple

crystalline Co-MOF precipitate were obtained, and collected by centrifugation, followed by washing with methanol and water multiple times.

2.2. Synthesis of Co-MOF-Urea

First, Co-MOF-OMS was prepared by activating Co-MOF at 155 °C under vacuum for 12 h. 2 g of urea was added to an H-tube and vacuum-dried for 12 h. Subsequently, 100 mg of Co-MOF-OMS was introduced into the H-tube in an Ar-filled glove box and subjected to heating at 135 °C for 24 h. The solid products were washed with ethanol for five times, then the Co-MOF-Urea was obtained.

2.3. Synthesis of $\text{Co}_{\text{SAs-NPs}}/\text{NC}$

100 mg of Co-MOF-Urea was placed in a quartz tube with continuous Ar flow (100 sccm), and heated at 700 °C for 2 h with a heating rate of $8 \text{ }^{\circ}\text{C min}^{-1}$. After cooling to room temperature, the powder products were subjected to a series of washing steps including 3 M HCl treatment at 85 °C for 12 h, rinsing with H_2O until a neutral pH was reached. Followed by vacuum drying overnight at 60 °C, the final $\text{Co}_{\text{SAs-NPs}}/\text{NC}$ product was obtained.

2.4. Synthesis of $\text{Co}_{\text{SAs}}/\text{NC}$

The synthesis of $\text{Co}_{\text{SAs}}/\text{NC}$ was conducted using an isostructural bimetallic MgCo -MOF precursor, which was synthesized in a similar manner to the Co-MOF with 5 mg of $\text{C}_4\text{H}_6\text{CoO}_4 \cdot 4\text{H}_2\text{O}$ and 25 mg of $\text{Mg}(\text{NO}_3)_2 \cdot 6\text{H}_2\text{O}$ in the first step. Then, MgCo -MOF-Urea was prepared following the same method used to synthesize Co-MOF-Urea. Next, 100 mg of MgCo -MOF-Urea was placed in a quartz tube with continuous Ar flow (100 sccm), and heated at 700 °C for 2 h with a heating rate of $8 \text{ }^{\circ}\text{C min}^{-1}$. After cooling to room temperature, the powder products were subjected to a series of washing steps including 3 M HCl treatment at 85 °C for 24 h to completely remove the Mg metal particles, rinsing with H_2O until a neutral pH was reached, and three rounds of ethanol wash. Followed by vacuum drying overnight at 60 °C, the final $\text{Co}_{\text{SAs}}/\text{NC}$ product was obtained.

2.5. Synthesis of $\text{Co}_{\text{NPs}}/\text{NC}$

$\text{Co}_{\text{NPs}}/\text{NC}$ was prepared by loading the Co-MOF-Urea precursor into a quartz tube, continuously ventilating argon (100 sccm), and heating at 1000 °C for 2 h at a heating rate of $8 \text{ }^{\circ}\text{C min}^{-1}$.

2.6. Synthesis of $\text{Co}_{\text{NPs}}/\text{C}$

$\text{Co}_{\text{NPs}}/\text{C}$ was prepared using similar preparation method to that of $\text{Co}_{\text{NPs}}/\text{NC}$ by replacing Co-MOF-Urea with Co-MOF.

3. Result and discussion

3.1. Synthesis and characterization

A schematic diagram illustrating the preparation process of $\text{Co}_{\text{SAs-NPs}}/\text{NC}$ is depicted in Fig. 1a. Briefly, the columnar material $\text{Co}_2(\text{dobpd})$ (Co-MOF) with hexagonal cross-section was prepared by dissolving cobalt acetate and 4,4'-dihydroxy-(1,1'-biphenyl)-3,3'-dicarboxylate (dobpd $^{4-}$) in a mixture of methanol, tetrahydrofuran and ultrapure water under vigorous stirring followed by hydrothermal reaction at 100 °C (Fig. S1). Subsequently, urea was introduced into the activated solvent-free coordination OMS Co-MOF framework [34,35]. Powder X-ray diffraction (PXRD) characterization revealed the presence of a distinct diffraction peak at 8.14° corresponding to the (300) plane in both pristine and urea-coordinated Co-MOF samples. This finding is consistent with simulated patterns and confirms the high purity and crystallinity of the coordination polymer (Fig. S2). Furthermore,

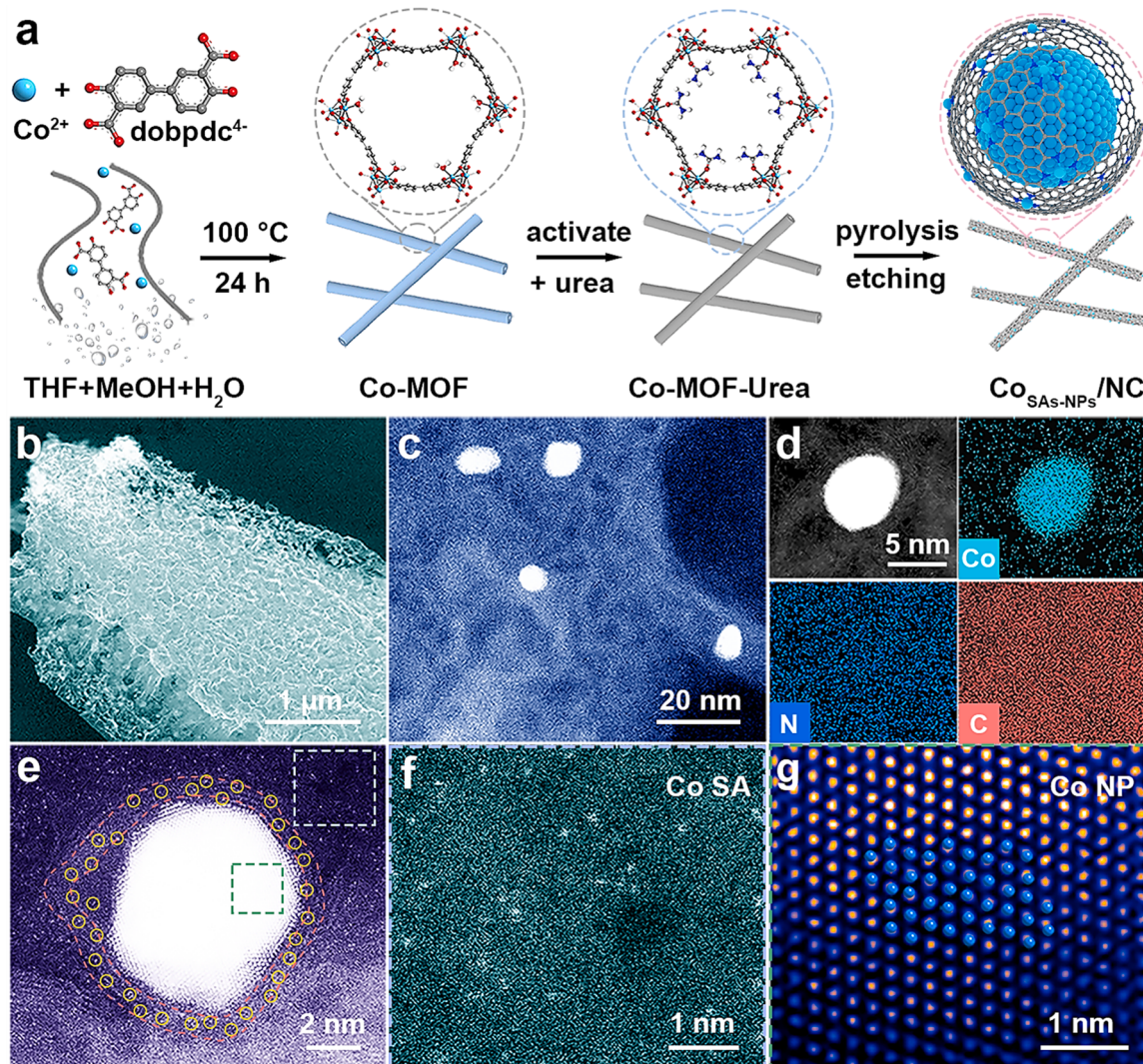


Fig. 1. Synthesis and microscopic characterizations of $\text{Co}_{\text{SAs-NPs}}/\text{NC}$. (a) Schematic illustration of the synthesis of $\text{Co}_{\text{SAs-NPs}}/\text{NC}$; (b) SEM image, (c) HAADF-STEM image, (d) high-resolution HAADF-STEM-EDS mappings of $\text{Co}_{\text{SAs-NPs}}/\text{NC}$; (e) Aberration-corrected (AC) HAADF-STEM image showing Co NP engaed in single-atom-dispersed graphite nanopocket; (f) AC-HAADF-STEM image showing abundant Co single atoms in $\text{Co}_{\text{SAs-NPs}}/\text{NC}$; (g) Atomic-resolution AC-HAADF-STEM image of the Co NP in $\text{Co}_{\text{SAs-NPs}}/\text{NC}$ showing the matched lattice with the (111) plane of cubic phase Co.

Fourier-transform infrared (FTIR) confirmed that the $\text{C}=\text{O}$ stretching frequency of ligated urea (1665 cm^{-1}) in Co-MOF-Urea is lower than that of free urea (1683 cm^{-1}), indicating coordination through the oxygen site (Fig. S3) [36]. Co-MOF-Urea was pyrolyzed at $700 \text{ }^\circ\text{C}$ under a N_2 atmosphere, and the large amount of Co-NPs on the exfoliated surfaces were efficiently removed by a simple acid-etching, yielding the targeted $\text{Co}_{\text{SAs-NPs}}/\text{NC}$. During high-temperature carbonization, the coordinated urea molecules acted as auxiliary nitrogen sources, effectively preventing the aggregation of Co-NPs and facilitating the formation of $\text{Co}-\text{N}_x$ SA sites. Thermal gravimetric analysis (TGA) indicates destruction of Co-MOF-Urea at $700 \text{ }^\circ\text{C}$ (Fig. S4), leading to a three-dimensional porous carbon structure which was also confirmed by scanning electron microscopy (SEM) images (Fig. 1b and Fig. S5).

Aberration-corrected transmission electron microscopy (AC-STEM) is employed to further analyze the morphology and microstructure of $\text{Co}_{\text{SAs-NPs}}/\text{NC}$. As shown in Fig. 1c, $\text{Co}_{\text{SAs-NPs}}/\text{NC}$ exhibits a three-dimensional porous carbon morphology, indicating its abundant pore structure. The porous properties facilitate mass transport during the ORR process [37,38]. Furthermore, the presence of Co-NPs with small sizes within the carbon matrix is also observed [39–41]. This phenomenon is mainly attributed to small-scale agglomeration caused by

insufficient stability and partial loss of N dopants at elevated temperatures [42]. From the energy dispersive spectrum elemental mapping presented herein, it is evident that Co, N, and C signals remain uniformly dispersed except for the more pronounced Co signal aggregation at particles interfaces. Moreover, atomic levels analysis reveals close proximity between Co–N signals suggests coexistence of both Co-NPs and Co-SAs in $\text{Co}_{\text{SAs-NPs}}/\text{NC}$ (Fig. 1d) [6,21]. The high-angle annular dark-field scanning transmission electron microscopy (HAADF-STEM) images further confirm this observation (Fig. 1e, f and Fig. S6). The graphite carbon layers surrounding the Co-NPs in $\text{Co}_{\text{SAs-NPs}}/\text{NC}$ contain numerous Co-SAs (yellow circles), creating an enclosure-like structure for the Co-NP within a graphite nanopocket. The graphite nanopockets observed were generated during the high-temperature pyrolysis of Co-MOF-urea. In this process, the formation of Co-NPs drives the graphitization of the surrounding carbon matrix, resulting in Co-NPs being encapsulated within highly graphitized carbon layers. In the meantime, the deep decomposition of urea-derived compounds produces substantial gaseous CN_x molecules, leading to expansion of the graphitic carbon layers. This process ultimately results in the formation of a nanopocket-like graphitic carbon layer structure within which Co-NPs are encapsulated. Such a local three-dimensional wrapping

coordination environment enables a higher number of interaction sites between the two entities, Co-SAs and Co-NPs, which is conducive to the enhancement of the catalyst activity. Notably, the graphite nanopocket could ensure tight protection for the encapsulated Co-NP in the long-term electrocatalysis (Fig. S7). In addition, the theoretical atomic model of cubic phase Co overlaps well with the actual atomic positions of metallic Co (blue atoms) in the (111) plane with a lattice distance of 0.206 nm (Fig. 1g and Fig. S8). The obtained results suggest the successful synthesis of a hybrid catalyst comprising of Co-SAs and ultrafine Co-NPs, which are respectively located on and within the nanopocket of N-doped graphite layers. For comparison purposes, we also conducted thermal decomposition of Co-MOF and Co-MOF-Urea, resulting in the preparation of carbon nanomaterials loaded with Co-NPs (Co_{NPs}/C) and N-doped carbon nanomaterials loaded with Co-NPs (Co_{NPs}/NC). In contrast, both the Co_{NPs}/NC and Co_{NPs}/C samples exhibit significant aggregation of metal atoms, indicating the presence of large-sized Co-NPs (Fig. S9 and S10).

The PXRD patterns in Fig. 2a reveal the presence of two sharp diffraction peaks at approximately 44.2° and 51.5° for both Co_{NPs}/NC and Co_{NPs}/C, corresponding to the (111) and (200) planes of Co. It is noteworthy that the intensity of the Co diffraction peak in Co_{NPs}/NC is significantly lower than that in Co_{NPs}/C due to the introduction of urea as N source during thermal decomposition process, which effectively prevented massive aggregation of Co atoms by anchoring them. It

directly proves that the interaction between the urea molecule and Co atoms during pyrolysis attenuates the agglomeration of Co atoms [43, 44]. In addition, the weak diffraction peaks of Co observed in Co_{SAs-NPs}/NC are mainly attributed to the removal of most of the Co-NPs during acid washing process. Raman spectroscopy was utilized to evaluate the relative calculated intensity ratios (I_D/I_G) between defect-related D-band (1338 cm⁻¹) and graphene-related G-band (1592 cm⁻¹) in the samples (Fig. 2b). The result demonstrates that Co_{SAs-NPs}/NC exhibits the largest I_D/I_G value of 1.03 among all samples, indicating a more favorable exposure of active sites. The higher defect peak intensity of Co_{SAs-NPs}/NC than that of Co_{SAs-NPs}/C primarily arises from the thermal decomposition of urea molecules in its precursor, which generates ammonia gas during high-temperature pyrolysis and etches the carbon matrix. Consequently, this phenomenon leads to a proliferation of numerous carbon defects within the carbon matrix, and an increase in specific surface area as evidenced by N₂ sorption isotherm tests [13, 45]. The type-III isotherms of Co_{SAs-NPs}/NC, Co_{SAs}/NC, Co_{NPs}/NC, and Co_{NPs}/C show similar characteristics with calculated specific surface areas of 269.86, 207.58, 228.20, and 152.49 m² g⁻¹, respectively (Fig. S11 and Table S1). The large specific surface area of Co_{SAs-NPs}/NC is mainly attributed to the increased number of pores generated during acid washing and leaching of partial unstable Co-NPs. Additionally, the pore size distribution (PSD) curve confirms the presence of a micro-mesoporous structure in these samples (Fig. S12).

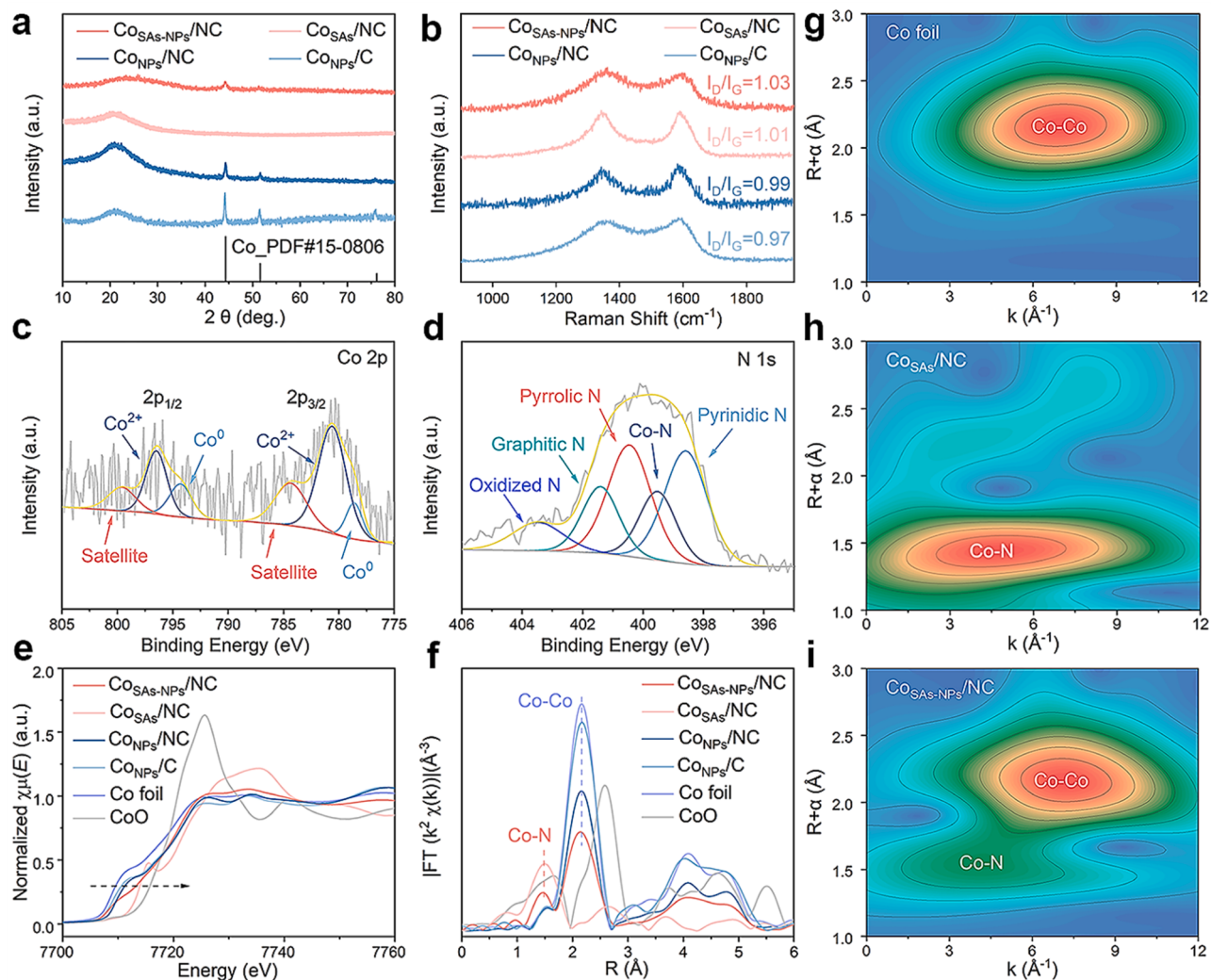


Fig. 2. Structural characterizations of catalysts. (a) PXRD patterns; (b) Raman spectra; (c) Deconvoluted Co 2p XPS for Co_{SAs-NPs}/NC; (d) High-resolution N 1 s XPS of Co_{SAs-NPs}/NC; (e) Co K-edge XANES spectra; (f) k²-weighted Fourier-transform EXAFS spectrum; (g–i) WT-EXAFS plots of Co foil, Co_{SAs}/NC, and Co_{SAs-NPs}/NC.

To determine the valence and chemical composition of the prepared catalysts, X-ray photoelectron spectroscopy (XPS) was performed. The XPS survey spectrum of $\text{Co}_{\text{SAs-NPs}}/\text{NC}$ reveals signals from C, N, and Co elements (Fig. S13). Further analysis of the high-resolution C 1 s spectra of all samples show sp^2 and sp^3 hybridized carbon species at 284.7 and 285.4 eV, respectively, along with others bound to oxygen (Fig. S14). In addition, in the high-resolution Co 2p XPS spectra (Fig. 2c), the peaks at 778.8 and 794.8 eV are assigned to the Co 2p_{3/2} and Co 2p_{1/2} spin-orbit states of the metallic Co⁰ species, respectively. Similarly, the peaks at 780.6 and 796.5 eV are assigned to the Co 2p_{3/2} and Co 2p_{1/2} spin-orbit states of the metallic Co²⁺ species, respectively. While the peaks at 784.3 and 799.5 eV are dithered satellite peaks. The deconvolution of the high-resolution N 1 s spectra reveals five characteristic peaks located at 398.7, 399.5, 400.5, 401.4, and 403.4 eV corresponding to pyridinic N, monoatomic Co sites bonded N (Co–N), pyrrolic N, graphitic N, and oxidized N, respectively (Fig. 2d) [46,47]. The presence of Co–N peak observed at 399.5 eV confirms the presence of Co–N_x single atom sites in the $\text{Co}_{\text{SAs-NPs}}/\text{NC}$ catalyst.

To verify the electronic structure and coordination environment of the Co species, various methods were employed. X-ray absorption near-edge structure (XANES) spectra of the samples were collected, and extended X-ray absorption fine structure (EXAFS) spectroscopy was conducted. In addition, reference analysis was performed using Co foil and CoO. The obtained Co K-edge XANES spectra show that the valence state of Co species in $\text{Co}_{\text{SAs-NPs}}/\text{NC}$ ranges from 0 to +2 (Fig. 2e), which is inferred from its near-edge absorption between the spectra of pure metallic Co foil and CoO [48,49]. The Co K-edge Fourier transform EXAFS (FT EXAFS) spectra of $\text{Co}_{\text{SAs-NPs}}/\text{NC}$ further indicate the appearance of two signal peaks at scattering paths around 1.45 and 2.15 Å, corresponding to the Co–N and metallic Co–Co signals, respectively, confirming the coexistence of Co-SAs with Co-NPs (Fig. 2f), consistent with the results of high-resolution N 1 s and Co 2p XPS analysis. The relatively weak signal of Co–N pathway can be primarily attributed to the coexistence of Co–Co pathway with an excessively strong reflection signal, as previously reported [6]. Given the stronger

signal observed at the metallic Co–Co path, it can be inferred that Co-NPs exert an important influence on the material, thus corroborating the findings obtained through STEM analysis. As expected, the peak representing the first coordination shell for Co–N in $\text{Co}_{\text{SAs}}/\text{NC}$ appears at ca. 1.45 Å, which is in good agreement with the above results. Meanwhile, no corresponding signal peaks were observed in $\text{Co}_{\text{NPs}}/\text{NC}$ and $\text{Co}_{\text{NPs}}/\text{C}$. Instead, a signal peak around 2.15 Å appeared in close proximity to that of Co foil [20,50]. Furthermore, by utilizing FT EXAFS for fitting analysis of the first atomic shell layer located at ca. 1.45 Å path in $\text{Co}_{\text{SAs-NPs}}/\text{NC}$, the quantitative coordination number of Co atoms is determined as 3.6, indicating the presence of an atomically dispersed Co–N₄ coordination conformation with a high level of accuracy (Fig. S15 and Table S2). Wavelet transform EXAFS (WT-EXAFS) analysis of $\text{Co}_{\text{SAs-NPs}}/\text{NC}$ resulted in the detection of concentrated signal contours that exhibit a high degree of concordance with both Co foil and $\text{Co}_{\text{SAs}}/\text{NC}$ (Fig. 2g–i). This conclusively confirms that Co atoms are uniformly dispersed throughout both SAs and NPs morphologies within the structure of $\text{Co}_{\text{SAs-NPs}}/\text{NC}$.

3.2. Electrocatalytic ORR performance

The prepared catalysts were subjected to electrochemical study of their ORR performance using a standard three-electrode system in 0.1 M KOH solution. By employing rotating ring-disk electrode (RRDE) and cyclic voltammetry (CV) measurements, it is apparent that all samples exhibit significant cathodic reduction peaks under O₂-saturated electrolytes as opposed to N₂-saturated electrolytes, thereby suggesting their activity in oxygen reduction (Fig. S16). Linear scanning voltammetry (LSV) curves demonstrate a low catalytic activity of $\text{Co}_{\text{NPs}}/\text{C}$, as evidenced by a half-wave potential ($E_{1/2}$) of 0.786 V (Fig. 3a). Upon introduction of the N source, the $E_{1/2}$ of $\text{Co}_{\text{NPs}}/\text{NC}$ (0.829 V) is right-shifted and the ORR performance is improved. Moreover, the $\text{Co}_{\text{SAs-NPs}}/\text{NC}$ exhibits a conspicuously enhanced $E_{1/2}$ of 0.871 V, outperforming that of commercial Pt/C (0.862 V), which can be attributed to the synergistic catalytic effect between Co-NPs and a substantial

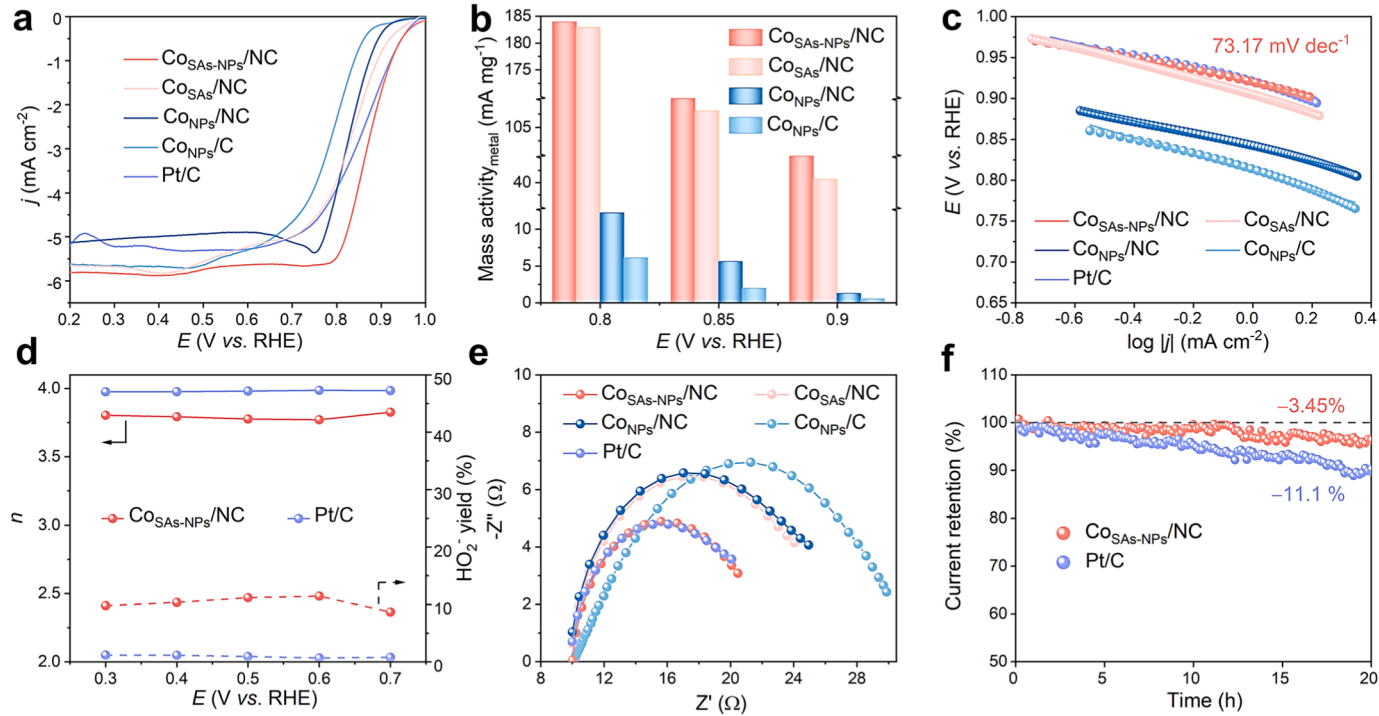


Fig. 3. ORR electrocatalytic performance. (a) Electrochemical oxygen reduction polarization curves at a rotation of 1600 rpm; (b) Metal-based mass activity comparison of different samples; (c) Tafel slopes of different samples and Pt/C; (d) H_2O_2 yield and electron transfer number of $\text{Co}_{\text{SAs-NPs}}/\text{NC}$ and Pt/C; (e) EIS of different samples and Pt/C; (f) Chronoamperometric curves of $\text{Co}_{\text{SAs-NPs}}/\text{NC}$ and Pt/C.

quantity of Co-SAs active species in the vicinity. Similarly, $\text{Co}_{\text{SAs-NPs}}/\text{NC}$ also demonstrates the largest limiting current density ($J_{\text{k}} = 5.81 \text{ mA cm}^{-2}$), superior to $\text{Co}_{\text{SAs}}/\text{NC}$ (5.66 mA cm^{-2}), $\text{Co}_{\text{NPs}}/\text{NC}$ (5.13 mA cm^{-2}), $\text{Co}_{\text{NPs}}/\text{C}$ (5.63 mA cm^{-2}), and Pt/C (5.18 mA cm^{-2}). This is mainly attributed to the strong catalytic synergy triggered by the unique “ship in a bottle” structure by encaging the Co-NPs into the Co-SAs-decorated graphite nanopockets [51]. It is worth mentioning that the exceptional ORR catalytic ability of $\text{Co}_{\text{SAs-NPs}}/\text{NC}$ is comparable to, or even superior to most cutting-edge non-precious metal catalysts

reported (Table S3). To further analyze the relationship between metal content and catalytic activity, the mass activities based on Co metals were analyzed (Fig. 3b). Among these catalysts, $\text{Co}_{\text{SAs-NPs}}/\text{NC}$ exhibits the highest mass activity with metal activity masses of 183.9, 127.5, and 58.7 mA mg^{-1} at 0.8, 0.85, and 0.90 V, respectively. These values are significantly higher than those observed for $\text{Co}_{\text{SAs}}/\text{NC}$ (182.9, 108.1, and 40.6 mA mg^{-1}), $\text{Co}_{\text{NPs}}/\text{NC}$ (12.2, 5.6, and 1.6 mA mg^{-1}), and $\text{Co}_{\text{NPs}}/\text{C}$ (6.1, 1.5, and 0.5 mA mg^{-1}). These results demonstrate that during the catalytic process, high atom utilization efficiency and catalytic activity

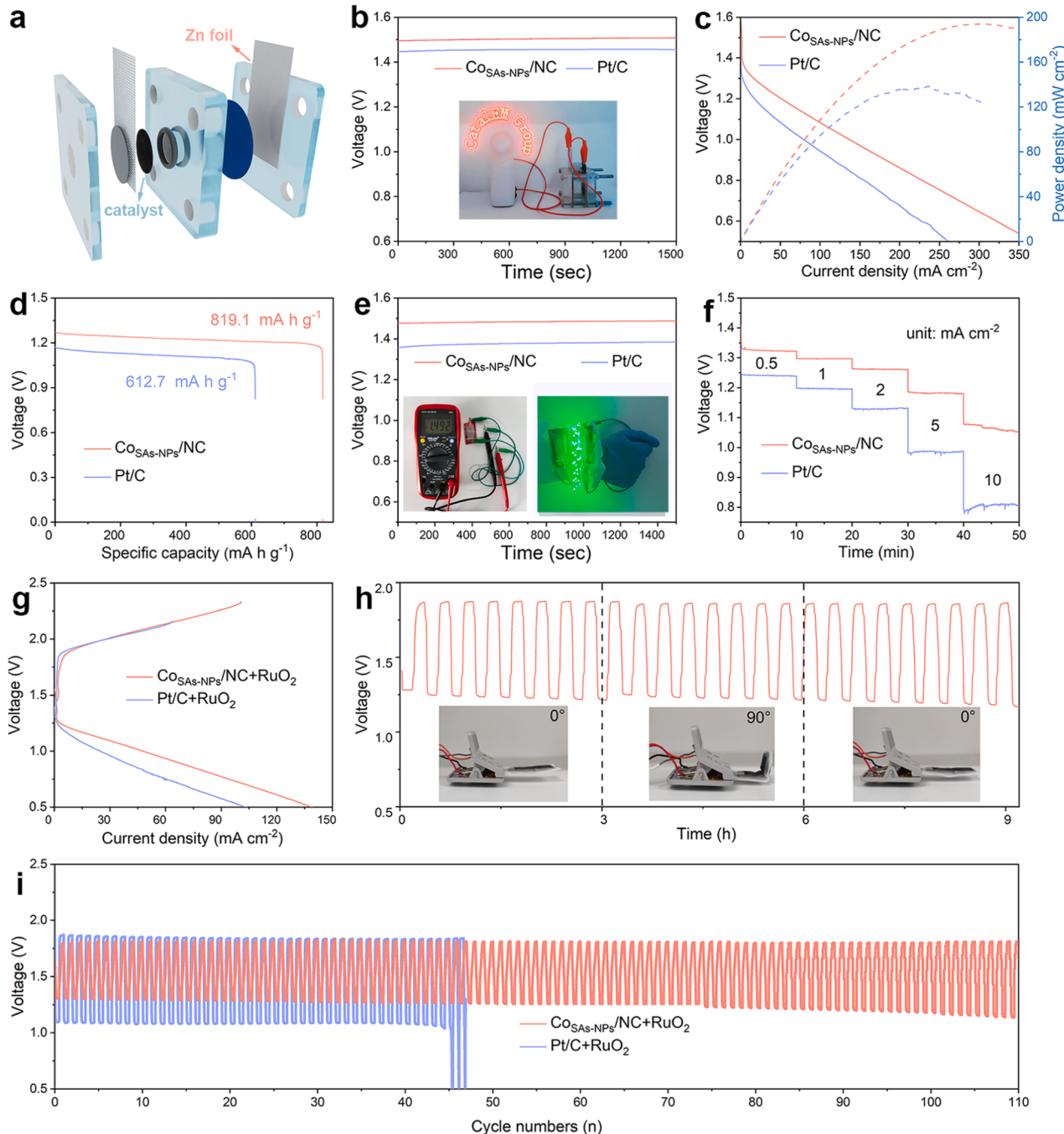


Fig. 4. ZAB performance tests. (a) Schematic diagram of a home-made liquid primary ZAB; (b) Open-circuit plots of liquid primary ZABs. Inset is a photograph showing “CatalEM Group” pattern on a fan driven by a liquid primary ZAB with $\text{Co}_{\text{SAs-NPs}}/\text{NC}$ as the air cathode; (c) Polarization and power density curves of liquid primary ZABs; (d) Specific capacity of the liquid primary ZABs; (e) Open-circuit plots of solid-state rechargeable ZABs; (f) Discharge curves of solid-state rechargeable ZABs at various current densities; (g) Charge and discharge polarization curves of solid-state rechargeable ZABs; (h) Stability of the solid-state rechargeable ZABs at 1 mA cm^{-2} . Insets are photographs of the solid-state rechargeable ZABs at flat (0°)/ bent (90°)/ flat (0°) states; (i) Galvanostatic cycling stability of the solid-state rechargeable ZABs at 1 mA cm^{-2} .

are achieved by Co-SAs and small Co-NPs. The LSV curves at different rotational speeds ranging from 100 to 2500 rpm were obtained for all samples and Pt/C. Additionally, the corresponding Koutechy–Levich (K–L) plots that depend on the rotational speed, were analyzed to reflect the diffusion-controlled characteristics of ORR (Fig. S17 and S18). By comparing Tafel plots, it is observed that $\text{Co}_{\text{SAs-NPs}}/\text{NC}$ exhibits the smallest Tafel slope of $73.17 \text{ mV dec}^{-1}$, indicating excellent reaction kinetics for the ORR and the enhanced mass transport between the catalyst and electrolyte due to a large number of exposed active sites (Fig. 3c) [52,53]. Furthermore, $\text{Co}_{\text{SAs-NPs}}/\text{NC}$ demonstrate an average electron transfer number (n) of 3.79 and a hydrogen peroxide yield of 10.01%, thus confirming its quasi-four electron pathway (Fig. 3d). The electrochemical double-layer capacitance (C_{dl}) of the sample was determined using the CV technique within the potential range of 0.99 to 1.09 V. Notably, $\text{Co}_{\text{SAs-NPs}}/\text{NC}$ exhibit the highest C_{dl} value of 38.51 mF cm^{-2} , surpassing that of the $\text{Co}_{\text{SAs}}/\text{NC}$ (19.62 mF cm^{-2}), $\text{Co}_{\text{NPs}}/\text{NC}$ (19.95 mF cm^{-2}), $\text{Co}_{\text{NPs}}/\text{C}$ (25.93 mF cm^{-2}), and Pt/C (31.31 mF cm^{-2}), as depicted in Fig. S19. The ORR kinetics of these catalysts were assessed through further analysis utilizing electrochemical impedance spectroscopy (EIS) (Fig. 3e). The semicircle diameter in the high frequency region indicates a lower charge transfer resistance (10.8Ω) of $\text{Co}_{\text{SAs-NPs}}/\text{NC}$, which is beneficial for fast electron transfer (Table S4). As shown in Fig. 3f, $\text{Co}_{\text{SAs-NPs}}/\text{NC}$ exhibits excellent stability with only a 3.5% decay in current retention after continuous reaction of 20 h, surpassing that of Pt/C (11.5%). The slower decline suggests the robust synergistic relationship between the surface Co-SAs active sites and the encaged inner Co-NPs stabilized and protected by the graphite nanopocket, which inhibits their aggregation and corrosion during the electrocatalytic process. Moreover, during methanol crossover testing, $\text{Co}_{\text{SAs-NPs}}/\text{NC}$ exhibited minimal current decay, while Pt/C exhibited an immediate and sharp current decay (Fig. S20).

3.3. Zn-air battery performance

To evaluate the feasibility of the $\text{Co}_{\text{SAs-NPs}}/\text{NC}$ catalyst in practical applications, a home-made liquid electrolyte ZAB was assembled and subjected for performance test. As shown in Fig. 4a, the liquid primary ZAB consists of a Zn plate as the anode, $\text{Co}_{\text{SAs-NPs}}/\text{NC}$ as the cathode exposed to ambient condition, and a 6.0 M KOH solution containing 0.2 M zinc acetate as electrolyte for ensuring a high ionic conductivity. For better comparison, ZAB with commercial Pt/C as the air cathode was tested under identical conditions. In Fig. 4b, the $\text{Co}_{\text{SAs-NPs}}/\text{NC}$ -based ZAB (denoted as $\text{Co}_{\text{SAs-NPs}}/\text{NC@ZAB}$) shows an open-circuit voltage (OCV) of 1.509 V, better than that of Pt/C-based ZAB (Pt/C@ZAB) (1.453 V). In addition, the inset showcases a fan with the “CatalEM Group” pattern can be directly powered by $\text{Co}_{\text{SAs-NPs}}/\text{NC@ZAB}$, demonstrating its potential application in energy conversion devices. Notably, as shown in Fig. 4c, $\text{Co}_{\text{SAs-NPs}}/\text{NC@ZAB}$ exhibits a considerable peak power density of 193.8 mW cm^{-2} , outperforming Pt/C@ZAB (138.2 mW cm^{-2}) and most of the previously reported ZABs (Table S5). Moreover, at a discharge current density of 10 mA cm^{-2} , $\text{Co}_{\text{SAs-NPs}}/\text{NC@ZAB}$ maintains a higher specific capacity ($819.1 \text{ mAh g}_{\text{Zn}}^{-1}$) than Pt/C@ZAB ($612.7 \text{ mAh g}_{\text{Zn}}^{-1}$) (Fig. 4d). The discharge potential plateaus of $\text{Co}_{\text{SAs-NPs}}/\text{NC@ZAB}$ were all higher than Pt/C@ZAB when the current density was gradually increased from 5 to 10, 20, 40, 60, and 80 mA cm^{-2} (Fig. S21). Even at a high current density of 80 mA cm^{-2} , $\text{Co}_{\text{SAs-NPs}}/\text{NC@ZAB}$ still exhibits an excellent high-rate performance with a high discharge potential of 1.01 V. The aforementioned results demonstrate the superiority of $\text{Co}_{\text{SAs-NPs}}/\text{NC@ZAB}$, thereby offering valuable insights and reference for future advancements in battery energy systems with their exceptional peak power density and ultra-high specific capacity.

To further demonstrate the promising application prospect of $\text{Co}_{\text{SAs-NPs}}/\text{NC}$ as an air cathode in alkaline ZAB, flexible solid-state ZAB using alkaline gel as a solid electrolyte was also assembled and tested. As shown in Fig. 4e, solid-state $\text{Co}_{\text{SAs-NPs}}/\text{NC@ZAB}$ exhibits a stable and excellent OCV of 1.492 V, which is higher than that of solid-state Pt/

C@ZAB (1.388 V). The trapezoidal discharge curves at different current densities ranging from 0.5 to 10 mA cm^{-2} further indicate that the solid-state $\text{Co}_{\text{SAs-NPs}}/\text{NC@ZAB}$ has a higher discharge plateau than the solid-state Pt/C@ZAB (Fig. 4f), especially at high current densities, suggesting that $\text{Co}_{\text{SAs-NPs}}/\text{NC@ZAB}$ holds a great potential for practical applications. Moreover, the peak power density of solid-state $\text{Co}_{\text{SAs-NPs}}/\text{NC@ZAB}$ reaches 73.4 mW cm^{-2} , surpassing that of Pt/C@ZAB (52.1 mW cm^{-2}) (Fig. S22). To further investigate the performance advantages of $\text{Co}_{\text{SAs-NPs}}/\text{NC}$ during charging and discharging, rechargeable solid-state ZAB was assembled by mixing $\text{Co}_{\text{SAs-NPs}}/\text{NC}$ and RuO_2 as the air cathodes (denoted as $\text{Co}_{\text{SAs-NPs}}/\text{NC+RuO}_2@\text{ZAB}$). For comparison, mixed commercial Pt/C and RuO_2 will also be tested as an air cathode to assemble a rechargeable solid-state ZAB. As shown in Fig. 4g, the charge/discharge voltage gap of $\text{Co}_{\text{SAs-NPs}}/\text{NC+RuO}_2@\text{ZAB}$ is much smaller than that of Pt/C+ $\text{RuO}_2@\text{ZAB}$ under the same current density, indicating superior ORR activity exhibited by $\text{Co}_{\text{SAs-NPs}}/\text{NC}$. In addition, solid-state $\text{Co}_{\text{SAs-NPs}}/\text{NC+RuO}_2@\text{ZAB}$ s also demonstrate a cycle-stable charge/discharge process lasting over 9 h in repetitive flat (0°)/bent (90°)/flat (0°) states (Fig. 4h), showing significant promise for portable and flexible device applications. Moreover, $\text{Co}_{\text{SAs-NPs}}/\text{NC+RuO}_2@\text{ZAB}$ was subjected to continuous charging/discharging cycling at a current density of 1 mA cm^{-2} for 10 min per cycle, to evaluate its cycle stability. As shown in Fig. 4i, it exhibits stability beyond 110 cycles at 1 mA cm^{-2} , which is much longer than that of Pt/C+ $\text{RuO}_2@\text{ZAB}$ (45 cycles). Therefore, the above results substantiate the satisfactory battery performance of $\text{Co}_{\text{SAs-NPs}}/\text{NC}$ in both liquid and solid electrolytes, underscoring its great potential in energy storage devices [54,55].

3.4. DFT calculations

To gain further insights into the synergistic effect of Co–N₄ SAs and Co-NPs in enhancing the ORR activity of $\text{Co}_{\text{SAs-NPs}}/\text{NC}$, three simulated models Co–CoN₄@G, CoN₄@G, and Co@G were constructed for DFT calculations (Fig. S23). The optimized geometrical configurations of the four elementary oxygenated intermediates $^*\text{O}_2$, $^*\text{OOH}$, $^*\text{O}$, and $^*\text{OH}$ (* refers to the active sites) in four-electron ORR adsorbed on these models are illustrated in Fig. 5a, and Fig. S24–S26. Especially for Co–CoN₄@G model, the calculation results demonstrate that oxygenated intermediates adsorbed on Co–N₄ SA sites results in a more favorable ORR process, with all elementary steps occurring spontaneously at $U = 0 \text{ V}$. This is superior to that on Co-NP sites, which involves an uphill step. Based on the more favorable adsorption performance of Co–N₄ SA sites and the unique configuration of $\text{Co}_{\text{SAs-NPs}}/\text{NC}$, where Co NPs are encaged in graphite nanopockets with Co-SAs decorating their surfaces, we infer that the primary catalytic role is played by Co–N₄ SA site, which was chosen as the binding active site for subsequent calculations (Fig. S27). As shown in Fig. 5b, the exothermic nature of all four elementary reactions of ORR on Co–CoN₄@G and CoN₄@G at $U = 0 \text{ V}$ indicates the spontaneous progression of ORR. Conversely, the endothermic final step involved in the formation of OH[–] on Co@G suggests its inferior ORR activity compared to that of Co–CoN₄@G and CoN₄@G, thus affirming the higher efficiency of SA sites over the NP sites. When the potential increases to the equilibrium potential ($U = 1.23 \text{ V}$), the ORR free energy profile on Co@G exhibits a similar trend to that under $U = 0 \text{ V}$ (Fig. 5c) [56]. However, there is a significant increase in the energy barrier for the last OH[–] formation step. On the contrary, both Co–CoN₄@G and CoN₄@G exhibit noticeable alterations in their free energy profiles under $U = 1.23 \text{ V}$, characterized by two or three endothermic steps, with the highest uphill free energy step corresponding to the rate-determining step (RDS) in ORR. As calculated, the RDS for all three models are found to be the last electron transfer step, which involves the desorption of OH intermediate to form the OH[–] product ($^*\text{OH} + \text{e}^- \rightarrow \text{OH}^-$) [57,58]. And the calculated energy barriers of RDS are 0.53, 0.7 and 2.15 eV for Co–CoN₄@G, CoN₄@G, and Co@G, respectively. The smaller free energy barrier on Co–CoN₄@G than that of CoN₄@G implies a weaker interaction with $^*\text{OH}$, leading to the enhanced

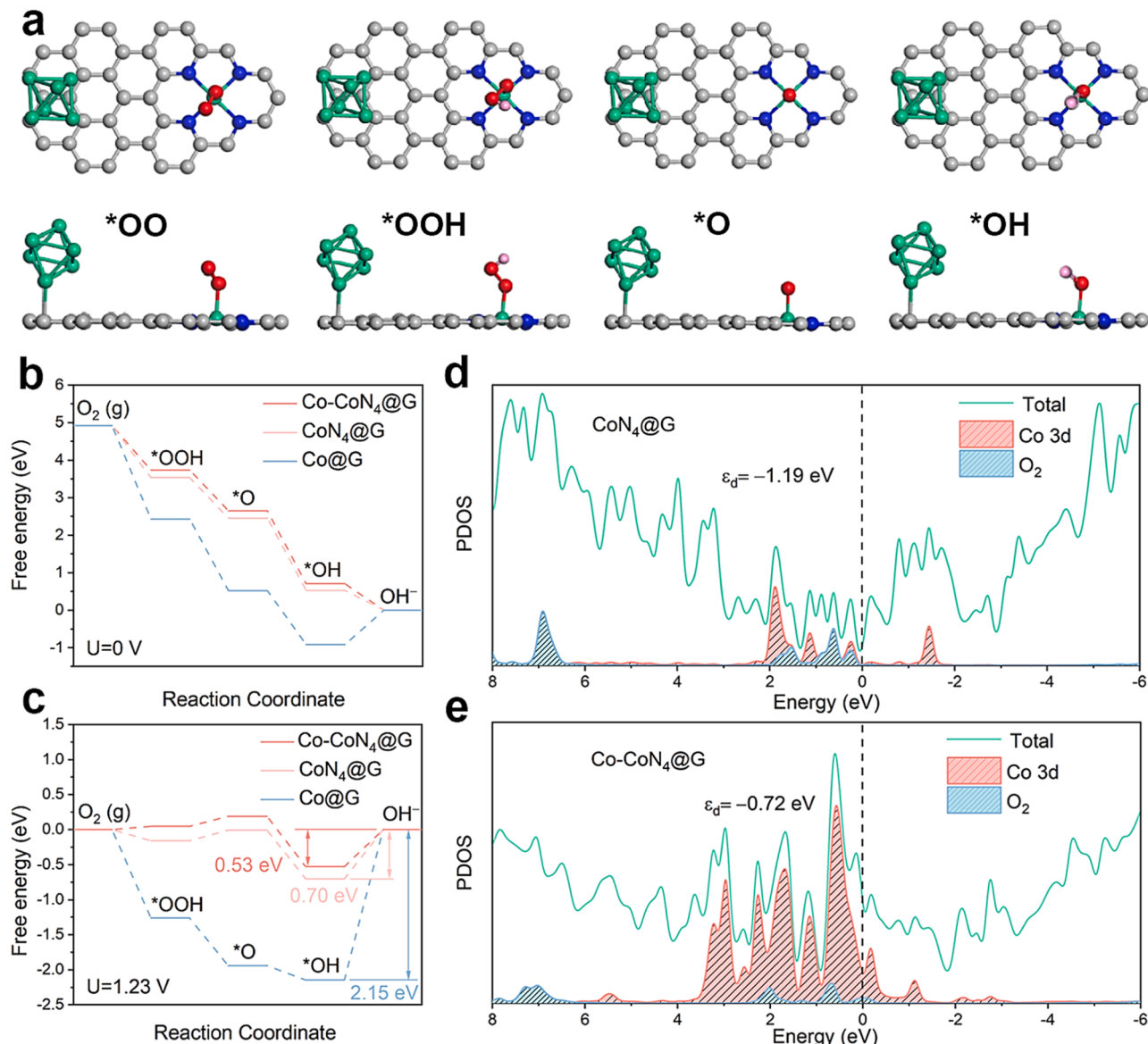


Fig. 5. DFT calculations of ORR on Co-CoN₄@G, CoN₄@G, and Co@G models. (a) The optimized geometrical structures of O-containing intermediates on CoN₄@G; (b) Gibbs free energy plots of ORR at U = 0 V; (c) Gibbs free energy plots of ORR at U = 1.23 V; (d) PDOS plot of O atoms on CoN₄@G; (e) PDOS plot of O atoms on Co-CoN₄@G.

ORR reaction kinetics and consequently superior activity, which aligns with the experimental observations. The obtained result provides rational evidence for the presence of synergistic coupling between Co-SAs and Co-NPs, which effectively enhances the ORR activity of Co_{SAs-NPs}/NC. To further elucidate the nature of synergy, the projected partial density of states (PDOS) of Co-CoN₄@G and CoN₄@G models upon O₂ adsorption on their surfaces are analyzed. As depicted in Figs. 5d and 5e, both Co-CoN₄@G and CoN₄@G exhibit orbit overlap between Co 3d-orbits and O₂ molecular orbitals, indicating their ability towards O₂ adsorption. However, it is noteworthy that Co-CoN₄@G displays a significantly higher density state of d-orbit cross the Fermi level (E_F) compared to CoN₄@G. This observation suggests that electron transfer capability between the surface of Co_{SAs-NPs}/NC and the adsorbate is remarkably enhanced in case of Co_{SAs-NPs}/NC, thereby optimizing the electrocatalytic reaction. Moreover, the d-band centers (ε_d) of Co-CoN₄@G and CoN₄@G are calculated to be -0.72 eV and -1.19 eV, respectively. According to the d-band center theory [59], a more negative value of the d-band center will lead to an increased filling of hybrid antibonding orbitals, resulting in the weakening of the interaction

between the catalyst reaction site and O-containing intermediates. Therefore, the upshifted d-band center closer to Fermi level in Co-CoN₄@G compared to that of CoN₄@G results in an enhanced binding strength toward intermediates, which is also supported by the large orbit overlap between Co 3d-orbitals and O₂ molecular orbitals observed in PDOS analysis. This enhancement in interaction contributes to the significant reduction in the energy barrier during the RDS for desorption of OH⁻ on Co-CoN₄@G, thereby promoting the ORR activity of Co_{SAs-NPs}/NC. Therefore, the theoretical calculation proves that the synergistic coupling of Co-SAs and NPs can optimize the electronic structure of the isolated Co-N₄ sites, leading to enhanced intrinsic catalyst activity and superior ORR performance.

4. Conclusion

Co_{SAs-NPs}/NC catalyst with intriguing nanostructure featuring Co-NP engaged in Co single atoms-dispersed graphite nanopocket has been successfully synthesized through an ingeniously designed MOF-route. The intimate building of the SA-decorated carbon wall around the Co-

NPs not only activate the full surface of Co-NPs for their maximum utilization as to create a strong synergistic coupling with surrounding isolated Co—N₄ sites, but also armors the Co-NP to prevent leaching and achieve stabilization of such synergy. Consequently, Co_{SAs-NPs}/NC exhibits remarkably outstanding ORR activity and stability under alkaline media, even surpassing commercial Pt/C benchmark. Moreover, the high catalytic capacity of Co_{SAs-NPs}/NC has been further showcased in both the liquid primary and flexible solid-state rechargeable ZABs with attractive battery performance. DFT calculations show that the close existence of a Co-NP effectively modulates the electronic structure of the Co—N₄ sites, resulting in an upshifted d-band center and thus the optimized adsorption toward the intermediates. Consequently, the energy barrier of the rate-determining step in ORR has been significantly decreased, which accelerates the O₂ reduction kinetics. This study provides valuable insights for designing more efficient and lasting synergistic effect in single-atom catalysis, and paving the way toward advanced electrocatalysts tailored for pragmatic energy conversion and storage devices.

CRediT authorship contribution statement

Shao Yu-Cheng: Data curation, Investigation, Resources. **Sun Chen:** Visualization. **Qian Jinjie:** Conceptualization, Methodology, Resources, Supervision, Validation, Writing – review & editing. **Chen Jeng-Lung:** Data curation, Resources, Writing – review & editing. **Han Lili:** Data curation, Formal analysis, Funding acquisition, Project administration, Resources, Validation, Writing – review & editing. **Yang Yuandong:** Data curation, Investigation, Methodology, Visualization, Writing – original draft. **Zhang Linjie:** Conceptualization, Methodology, Supervision, Validation, Writing – original draft, Writing – review & editing. **Xiao Yi:** Investigation, Methodology, Visualization. **Chen Kuan-Hung:** Data curation, Investigation. **Wang Hsiao-Tsu:** Data curation, Investigation, Resources. **Jin Na:** Formal analysis, Validation. **Lin Wei-Xuan:** Data curation, Investigation.

Declaration of Competing Interest

The authors declare that they have no known competing financial interests or personal relationships that could have appeared to influence the work reported in this paper.

Data Availability

Data will be made available on request.

Acknowledgement

This work was supported by the National Key Research & Development Program of China (2022YFA1505700, 2019YFA0210403), National Natural Science Foundation of China (22205232, 21601187, 21601137), Natural Science Foundation of Fujian Province (2023J06044, 2023J01213), and Fund for Distinguished Young Scholars of FJIRSM (CXZX-2022-JQ06). The XAFS spectra measurements on beamlines TPS 44 A and TLS 17 C at National Synchrotron Radiation Research Center (NSRRC) are greatly appreciated. The authors also acknowledge support by Transmission electron microscope platform and High-performance Computing Platform of Fujian Science & Technology Innovation Laboratory for Optoelectronic Information of China.

Appendix A. Supporting information

Supplementary data associated with this article can be found in the online version at [doi:10.1016/j.apcatb.2024.123792](https://doi.org/10.1016/j.apcatb.2024.123792).

References

- [1] L. Yang, X. Zhang, L. Yu, J. Hou, Z. Zhou, R. Lv, Atomic Fe–N₄/C in flexible carbon fiber membrane as binder-free air cathode for Zn-air batteries with stable cycling over 1000h, *Adv. Mater.* 34 (2022) 2105410, <https://doi.org/10.1002/adma.202105410>.
- [2] X. Zhong, Z. Zheng, J. Xu, X. Xiao, C. Sun, M. Zhang, J. Ma, B. Xu, K. Yu, X. Zhang, H.-M. Cheng, G. Zhou, Flexible zinc-air batteries with ampere-hour capacities and wide-temperature adaptabilities, *Adv. Mater.* 35 (2023) 2209980, <https://doi.org/10.1002/adma.202209980>.
- [3] J. Sun, H. Xue, L. Lu, M. Gao, N. Guo, T. Song, H. Dong, J. Zhang, L. Wu, Q. Wang, Atomic-level modulation of local coordination environment at Fe single-atom sites for enhanced oxygen reduction, *Appl. Catal. B* 313 (2022) 121429, <https://doi.org/10.1016/j.apcatb.2022.121429>.
- [4] Q. Shi, Y. He, X. Bai, M. Wang, D.A. Cullen, M. Lucero, X. Zhao, K.L. More, H. Zhou, Z. Feng, Y. Liu, G. Wu, Methanol tolerance of atomically dispersed single metal site catalysts: Mechanistic understanding and high-performance direct methanol fuel cells, *Energy Environ. Sci.* 13 (2020) 3544–3555, <https://doi.org/10.1039/D0EE01968B>.
- [5] Y. Yang, Q. Sun, J. Xue, S. Xu, L. Mao, T. Miao, L. Zhang, J. Qian, MOF-derived N-doped carbon nanosticks coupled with Fe phthalocyanines for efficient oxygen reduction, *Chem. Eng. J.* 464 (2023) 142668, <https://doi.org/10.1016/j.cej.2023.142668>.
- [6] Z. Wang, C. Zhu, H. Tan, J. Liu, L. Xu, Y. Zhang, Y. Liu, X. Zou, Z. Liu, X. Lu, Understanding the synergistic effects of cobalt single atoms and small nanoparticles: Enhancing oxygen reduction reaction catalytic activity and stability for zinc-air batteries, *Adv. Funct. Mater.* 31 (2021) 2104735, <https://doi.org/10.1002/adfm.202104735>.
- [7] X. Tian, X.F. Lu, B.Y. Xia, X.W. Lou, Advanced electrocatalysts for the oxygen reduction reaction in energy conversion technologies, *Joule* 4 (2020) 45–68, <https://doi.org/10.1016/j.joule.2019.12.014>.
- [8] P. Cui, L. Zhao, Y. Long, L. Dai, C. Hu, Carbon-based electrocatalysts for acidic oxygen reduction reaction, *Angew. e202218269*, *Chem. Int. Ed.* 62 (2023) 18269, <https://doi.org/10.1002/anie.2022>.
- [9] W. Peng, Y. Wang, X. Yang, L. Mao, J. Jin, S. Yang, K. Fu, G. Li, Co₉S₈ nanoparticles embedded in multiple doped and electrospun hollow carbon nanofibers as bifunctional oxygen electrocatalysts for rechargeable zinc-air battery, *Appl. Catal. B* 118437 (2019), <https://doi.org/10.1016/j.apcatb>.
- [10] L. Xue, Y. Li, X. Liu, Q. Liu, J. Shang, H. Duan, L. Dai, J. Shui, Zigzag carbon as efficient and stable oxygen reduction electrocatalyst for proton exchange membrane fuel cells, *Nat. Commun.* 9 (2018) 3819, <https://doi.org/10.1038/s41467-018-06279-x>.
- [11] Q. Yang, Y. Jia, F. Wei, L. Zhuang, D. Yang, J. Liu, X. Wang, S. Lin, P. Yuan, X. Yao, Understanding the activity of Co—N₄—C_x in atomic metal catalysts for oxygen reduction catalysis, *Angew. Chem. Int. Ed.* 59 (2020) 6122–6127, <https://doi.org/10.1002/anie.202000324>.
- [12] X. Tian, X. Zhao, Y.-Q. Su, L. Wang, H. Wang, D. Dang, B. Chi, H. Liu, E.J. M. Hensen, X.W. Lou, B.Y. Xia, Engineering bunched Pt–Ni alloy nanocages for efficient oxygen reduction in practical fuel cells, *Science* 366 (2019) 850–856, <https://doi.org/10.1126/science.aaw7493>.
- [13] Y. Yuan, Q. Zhang, Y. Li, L. Lv, Y. Hou, G. Li, J. Fu, L. Yang, Z. Bai, Beads-on-string hierarchical structured electrocatalysts for efficient oxygen reduction reaction, *Carbon Energy* 5 (2023) e253, <https://doi.org/10.1002/cey.2253>.
- [14] Y. Guo, C. Wang, Y. Xiao, X. Tan, J. Chen, W. He, Y. Li, H. Cui, C. Wang, Increasing the number of modulated Fe single-atom sites by adjacent nanoparticles for efficient oxygen reduction with spin-state transition, *Nano Energy* 117 (2023) 108895 <https://doi.org/10.1016/j.nanoen.2023.108895>.
- [15] L. Zong, K. Fan, W. Wu, L. Cui, L. Zhang, B. Johannessen, D. Qi, H. Yin, Y. Wang, P. Liu, L. Wang, H. Zhao, Anchoring single copper atoms to microporous carbon spheres as high-performance electrocatalyst for oxygen reduction reaction, *Adv. Funct. Mater.* 31 (2021) 2104864, <https://doi.org/10.1002/adfm.202104864>.
- [16] L. Han, H. Cheng, W. Liu, H. Li, P. Ou, R. Lin, H.-T. Wang, C.-W. Pao, A.R. Head, C.-H. Wang, X. Tong, C.-J. Sun, W.-F. Pong, J. Luo, J.-C. Zheng, H.L. Xin, A single-atom library for guided monometallic and concentration-complex multimetallic designs, *Nat. Mater.* 21 (2022) 681–688, <https://doi.org/10.1038/s41563-022-01252-y>.
- [17] P. Thangasamy, S. Oh, H. Randriamahazaka, S. Nam, I.-K. Oh, Mechanistic insight into collectively exhaustive CoPi-NPC nanosheets for oxygen reduction reaction and Zn-air battery, *Appl. Catal. B* 316 (2022) 121656, <https://doi.org/10.1016/j.apcatb.2022.121656>.
- [18] Q. Jin, C. Wang, Y. Guo, Y. Xiao, X. Tan, J. Chen, W. He, Y. Li, H. Cui, C. Wang, Axial oxygen ligands regulating electronic and geometric structure of Zn-N-C sites to boost oxygen reduction reaction, *Adv. Sci.* 10 (2023) 2302152, <https://doi.org/10.1002/advs.202302152>.
- [19] S. Chandrasekaran, R. Hu, L. Yao, L. Sui, Y. Liu, A. Abdelkader, Y. Li, X. Ren, L. Deng, Mutual self-regulation of d-electrons of single atoms and adjacent nanoparticles for bifunctional oxygen electrocatalysis and rechargeable zinc-air batteries, *Nano-Micro Lett.* 15 (2023) 48, <https://doi.org/10.1007/s40820-023-01022-8>.
- [20] S. Yuan, J. Zhang, L. Hu, J. Li, S. Li, Y. Gao, Q. Zhang, L. Gu, W. Yang, X. Feng, B. Wang, Decarboxylation-induced defects in MOF-derived single cobalt atom@carbon electrocatalysts for efficient oxygen reduction, *Angew. Chem. Int. Ed.* 60 (2021) 21685–21690, <https://doi.org/10.1002/anie.202107053>.
- [21] J. Zhang, Y. Xie, Q. Jiang, S. Guo, J. Huang, L. Xu, Y. Wang, G. Li, Facile synthesis of cobalt cluster-Co_N composites: synergistic effect boosts electrochemical oxygen

reduction, *J. Mater. Chem. A* 10 (2022) 16920–16927, <https://doi.org/10.1039/D2TA04413G>.

[22] N.R. Sahraei, U.I. Kramm, J. Steinberg, Y. Zhang, A. Thomas, T. Reier, J.-P. Paraknowitsch, P. Strasser, Quantifying the density and utilization of active sites in non-precious metal oxygen electroreduction catalysts, *Nat. Commun.* 6 (2015) 8618, <https://doi.org/10.1038/ncomms9618>.

[23] C. Zhu, Q. Shi, B.Z. Xu, S. Fu, G. Wan, C. Yang, S. Yao, J. Song, H. Zhou, D. Du, S. P. Beckman, D. Su, Y. Lin, Hierarchically porous M–N–C (M = Co and Fe) single-atom electrocatalysts with robust MN_x active moieties enable enhanced ORR performance, *Adv. Energy Mater.* 8 (2018) 1801956, <https://doi.org/10.1002/aenm.201801956>.

[24] L. Yan, P. Li, Q. Zhu, A. Kumar, K. Sun, S. Tian, X. Sun, Atomically precise electrocatalysts for oxygen reduction reaction, *Chem* 9 (2023) 280–342, <https://doi.org/10.1016/j.chempr.2023.01.003>.

[25] P.-Q. Liao, J.-Q. Shen, J.-P. Zhang, Metal-organic frameworks for electrocatalysis, *Coord. Chem. Rev.* 373 (2018) 22–48, <https://doi.org/10.1016/j.ccr.2017.09.001>.

[26] I.E. Khalil, J. Fonseca, M.R. Reithofer, T. Eder, J.M. Chin, Tackling orientation of metal-organic frameworks (MOFs): The quest to enhance MOF performance, *Coord. Chem. Rev.* 481 (2023) 215043, <https://doi.org/10.1016/j.ccr.2023.215043>.

[27] J. Tian, F. Jiang, D. Yuan, L. Zhang, Q. Chen, M. Hong, Electric-field assisted *in situ* hydrolysis of bulk metal-organic frameworks (MOFs) into ultrathin metal oxyhydroxide nanosheets for efficient oxygen evolution, *Angew. Chem. Int. Ed.* 59 (2020) 13101–13108, <https://doi.org/10.1002/anie.202004420>.

[28] X. Li, X. Yang, L. Liu, H. Zhao, Y. Li, H. Zhu, Y. Chen, S. Guo, Y. Liu, Q. Tan, G. Wu, Chemical vapor deposition for N/S-doped single Fe site catalysts for the oxygen reduction in direct methanol fuel cells, *ACS Catal.* 11 (2021) 7450–7459, <https://doi.org/10.1021/acscatal.0c05446>.

[29] Y. Wang, R. Gan, H. Liu, M. Dirican, C. Wei, C. Ma, J. Shi, X. Zhang, Fe₃O₄/Fe₂O₃/Fe nanoparticles anchored on N-doped hierarchically porous carbon nanospheres as a high-efficiency ORR electrocatalyst for rechargeable Zn-air batteries, *J. Mater. Chem. A* 9 (2021) 2764–2774, <https://doi.org/10.1039/DOTA10205A>.

[30] X. Luo, C. Fu, S. Shen, L. Luo, J. Zhang, Free-templated synthesis of N-doped PtCu porous hollow nanospheres for efficient ethanol oxidation and oxygen reduction reactions, *Appl. Catal. B* 330 (2023) 122602, <https://doi.org/10.1016/j.apcatb.2023.122602>.

[31] L. Gong, J. Zhu, F. Xia, Y. Zhang, W. Shi, L. Chen, J. Yu, J. Wu, S. Mu, Marriage of ultralow platinum and single-atom Mn_N moiety for augmented ORR and HER catalysis, *ACS Catal.* 13 (2023) 4012–4020, <https://doi.org/10.1021/acscatal.2c06340>.

[32] B. Wang, M. Li, S. Zhang, H. Wu, Y. Liao, H. Li, Synergistic effect between Co single atoms and nanoparticles enables selective synthesis of bio-based benzimidazoles, *Appl. Catal. B* 327 (2023) 122454, <https://doi.org/10.1016/j.apcatb.2023.122454>.

[33] C. Fu, X. Qi, L. Zhao, T. Yang, Q. Xue, Z. Zhu, P. Xiong, J. Jiang, X. An, H. Chen, J. S. Chen, A. Cabot, R. Wu, Synergistic cooperation between atomically dispersed Zn and Fe on porous nitrogen-doped carbon for boosting oxygen reduction reaction, *Appl. Catal. B* 335 (2023) 122875, <https://doi.org/10.1016/j.apcatb.2023.122875>.

[34] T.M. McDonald, J.A. Mason, X. Kong, E.D. Bloch, D. Gygi, A. Dani, V. Crocellà, F. Giordanino, S.O. Odoh, W.S. Drisdell, B. Vlaisavljevich, A.L. Dzubak, R. Poloni, S.K. Schnell, N. Planas, K. Lee, T. Pascal, L.F. Wan, D. Prendergast, J.B. Neaton, B. Smit, J.B. Kortright, L. Gagliardi, S. Bordiga, J.A. Reimer, J.R. Long, Cooperative insertion of CO₂ in diamine-appended metal-organic frameworks, *Nature* 519 (2015) 303–308, <https://doi.org/10.1038/nature14327>.

[35] E.J. Kim, R.L. Siegelman, H.Z.H. Jiang, A.C. Forse, J.-H. Lee, J.D. Martell, P. J. Milner, J.M. Falkowski, J.B. Neaton, J.A. Reimer, S.C. Weston, J.R. Long, Cooperative carbon capture and steam regeneration with tetraamine-appended metal-organic frameworks, *Science* 369 (2020) 392–396, <https://doi.org/10.1126/science.abb3976>.

[36] M.K. Sarango-Ramírez, J. Park, J. Kim, Y. Yoshida, D.-W. Lim, H. Kitagawa, Void space versus surface functionalization for proton conduction in metal-organic frameworks, *Angew. Chem. Int. Ed.* 60 (2021) 20173–20177, <https://doi.org/10.1002/anie.202106181>.

[37] M. Xiao, J. Zhu, G. Li, N. Li, S. Li, Z.P. Cano, L. Ma, P. Cui, P. Xu, G. Jiang, H. Jin, S. Wang, T. Wu, J. Lu, A. Yu, D. Su, Z. Chen, A single-atom iridium heterogeneous catalyst in oxygen reduction reaction, *Angew. Chem. Int. Ed.* 58 (2019) 9640–9645, <https://doi.org/10.1002/anie.201905241>.

[38] X. Xie, L. Shang, X. Xiong, R. Shi, T. Zhang, Fe single-atom catalysts on MOF-5 derived carbon for efficient oxygen reduction reaction in proton exchange membrane fuel cells, *Adv. Energy Mater.* 12 (2022) 2102688, <https://doi.org/10.1002/aenm.202102688>.

[39] K. Strickland, E. Miner, Q. Jia, U. Tylus, N. Ramaswamy, W. Liang, M.-T. Sougrati, F. Jaouen, S. Mukerjee, Highly active oxygen reduction non-platinum group metal electrocatalyst without direct metal–nitrogen coordination, *Nat. Commun.* 6 (2015) 7343, <https://doi.org/10.1038/ncomms8343>.

[40] X. Ding, C. Jia, P. Ma, H. Chen, J. Xue, D. Wang, R. Wang, H. Cao, M. Zuo, S. Zhou, Z. Zhang, J. Zeng, J. Bao, Remote synergy between heterogeneous single atoms and clusters for enhanced oxygen evolution, *Nano Lett.* 23 (2023) 3309–3316, <https://doi.org/10.1021/acs.nanolett.3c00228>.

[41] X. Zhou, K. Song, Y. Feng, C. Jiang, Z. Chen, Z. Wang, N. Yue, X. Ge, W. Zhang, W. Zheng, Individually-atomic governing d–π* orbital interactions via Cu-promoted optimization of Fe-d band centers for high-efficiency zinc-air battery, *Nano Res.* 16 (2023) 4634–4642, <https://doi.org/1.1007/s12274-022-5091-y>.

[42] J. Yang, W. Li, D. Wang, Y. Li, Single-atom materials: small structures determine macroproperties, *Small Struct.* 2 (2021) 2000051, <https://doi.org/10.1002/sstr.202000051>.

[43] L. Liang, H. Jin, H. Zhou, B. Liu, C. Hu, D. Chen, Z. Wang, Z. Hu, Y. Zhao, H.-W. Li, D. He, S. Mu, Cobalt single atom site isolated Pt nanoparticles for efficient ORR and HER in acid media, *Nano Energy* 88 (2021) 106221, <https://doi.org/10.1016/j.nanoen.2021.106221>.

[44] L. Li, N. Li, J. Xia, S. Zhou, X. Qian, F. Yin, G. He, H. Chen, Metal-organic framework-derived Co single atoms anchored on N-doped hierarchically porous carbon as a pH-universal ORR electrocatalyst for Zn-air, *Batter.*, *J. Mater. Chem. A* 11 (2023) 2291–2301, <https://doi.org/10.1039/D2TA08808H>.

[45] Y. Zhu, G. Li, D. Luo, H. Wan, M. Feng, D. Yuan, W. Hu, Z. Li, R. Gao, Z. Zhang, W. Liu, M. Li, Y. Deng, L. Wang, Y. Hu, X. Chen, Z. Chen, Unsaturated coordination polymer frameworks as multifunctional sulfur reservoir for fast and durable lithium-sulfur batteries, *Nano Energy* 79 (2021) 105393, <https://doi.org/10.1016/j.nanoen.2020.105393>.

[46] Y. He, H. Guo, S. Hwang, X. Yang, Z. He, J. Braaten, S. Karakalos, W. Shan, M. Wang, H. Zhou, Z. Feng, K.L. More, G. Wang, D. Su, D.A. Cullen, L. Fei, S. Listter, G. Wu, Single cobalt sites dispersed in hierarchically porous nanofiber networks for durable and high-power PGM-free cathodes in fuel cells, *Adv. Mater.* 32 (2020) 2003577, <https://doi.org/10.1002/adma.202003577>.

[47] L.-N. Song, W. Zhang, Y. Wang, X. Ge, L.-C. Zou, H.-F. Wang, X.-X. Wang, Q.-C. Liu, F. Li, J.-J. Xu, Tuning lithium–peroxide formation and decomposition routes with single-atom catalysts for lithium–oxygen batteries, *Nat. Commun.* 11 (2020) 2191, <https://doi.org/10.1038/s41467-020-15712-z>.

[48] W. Sun, L. Du, Q. Tan, J. Zhou, Y. Hu, C. Du, Y. Gao, G. Yin, Engineering of nitrogen coordinated single cobalt atom moieties for oxygen electroreduction, *ACS Appl. Mater. Interfaces* 11 (2019) 41258–41266, <https://doi.org/10.1021/acsami.9b11830>.

[49] Y. Chen, R. Gao, S. Ji, H. Li, K. Tang, P. Jiang, H. Hu, Z. Zhang, H. Hao, Q. Qu, X. Liang, W. Chen, J. Dong, D. Wang, Y. Li, Atomic-level modulation of electronic density at cobalt single-atom sites derived from metal-organic frameworks: Enhanced oxygen reduction performance, *Angew. Chem. Int. Ed.* 60 (2021) 3212–3221, <https://doi.org/10.1002/anie.202012798>.

[50] P. Yin, T. Yao, Y. Wu, L. Zheng, Y. Lin, W. Liu, H. Ju, J. Zhu, X. Hong, Z. Deng, G. Zhou, S. Wei, Y. Li, Single cobalt atoms with precise N-coordination as superior oxygen reduction reaction catalysts, *Angew. Chem. Int. Ed.* 55 (2016) 10800–10805, <https://doi.org/10.1002/anie.201604802>.

[51] Z. Zhao, Z. Liu, A. Zhang, X. Yan, W. Xue, B. Peng, H.L. Xin, X. Pan, X. Duan, Y. Huang, Graphene-nanopocket-encaged PtCo nanocatalysts for highly durable fuel cell operation under demanding ultralow-Pt-loading conditions, *Nat. Nanotechnol.* 17 (2022) 968–975, <https://doi.org/10.1038/s41565-022-01170-9>.

[52] G. Chen, Y. An, S. Liu, F. Sun, H. Qi, H. Wu, Y. He, P. Liu, R. Shi, J. Zhang, A. Kuc, U. Kaiser, T. Zhang, T. Heine, G. Wu, X. Feng, Highly accessible and dense surface single metal FeN₄ active sites for promoting the oxygen reduction reaction, *Energy Environ. Sci.* 15 (2022) 2619–2628, <https://doi.org/10.1039/D2EE00542E>.

[53] L. Zhang, T. Gu, K. Lu, L. Zhou, D.-S. Li, R. Wang, Engineering synergistic edge-N dipole in metal-free carbon nanoflakes toward intensified oxygen reduction electrocatalysis, *Adv. Funct. Mater.* 31 (2021) 2103187, <https://doi.org/10.1002/adfm.202103187>.

[54] J. Pan, Y.Y. Xu, H. Yang, Z. Dong, H. Liu, B.Y. Xia, Advanced architectures and relatives of air electrodes in Zn-air batteries, *Adv. Sci.* 5 (2018) 1700691, <https://doi.org/10.1002/advs.201700691>.

[55] Q. Wang, Q. Feng, Y. Lei, S. Tang, L. Xu, Y. Xiong, G. Fang, Y. Wang, P. Yang, J. Liu, W. Liu, X. Xiong, Quasi-solid-state Zn-air batteries with an atomically dispersed cobalt electrocatalyst and organohydrogel electrolyte, *Nat. Commun.* 13 (2022) 3689, <https://doi.org/10.1038/s41467-022-31383-4>.

[56] T. Gu, D. Zhang, Y. Yang, C. Peng, D. Xue, C. Zhi, M. Zhu, J. Liu, Dual-sites coordination engineering of single atom catalysts for full-temperature adaptive flexible ultralong-life solid-state Zn-air batteries, *Adv. Funct. Mater.* 33 (2023) 2212299, <https://doi.org/10.1002/adfm.202212299>.

[57] Y. Lian, W. Yang, C. Zhang, H. Sun, Z. Deng, W. Xu, L. Song, Z. Ouyang, Z. Wang, J. Guo, Y. Peng, Unpaired 3d electrons on atomically dispersed cobalt centres in coordination polymers regulate both oxygen reduction reaction (ORR) activity and selectivity for use in Zinc-air batteries, *Angew. Chem. Int. Ed.* 59 (2020) 286–294, <https://doi.org/10.1002/anie.201910879>.

[58] D. Deng, J. Qian, X. Liu, H. Li, D. Su, H. Li, H. Li, L. Xu, Non-covalent interaction of atomically dispersed Cu and Zn pair sites for efficient oxygen reduction reaction, *Adv. Funct. Mater.* 32 (2022) 2203471, <https://doi.org/10.1002/adfm.202203471>.

[59] B. Hammer, J.K. Nørskov, Electronic factors determining the reactivity of metal surfaces, *Surf. Sci.* 343 (1995) 211–220, [https://doi.org/10.1016/0039-6028\(95\)80007-0](https://doi.org/10.1016/0039-6028(95)80007-0).